Effects of particle size distribution and blast velocity on furnace raceway transport behaviors and dynamic characteristics using DEM-CFD

Li, Meng; Li, Chao; Wu, Guanyin; An, Xizhong; Zhang, Hao; Fu, Haitao; Yang, Xiaohong; Zou, Qingchuan; Wu, Yongli; Dong, Kejun

DOI
10.1016/j.apt.2024.104432

Publication date
2024

Document Version
Final published version

Published in
Advanced Powder Technology

Citation (APA)
Li, M., Li, C., Wu, G., An, X., Zhang, H., Fu, H., Yang, X., Zou, Q., Wu, Y., & Dong, K. (2024). Effects of particle size distribution and blast velocity on furnace raceway transport behaviors and dynamic characteristics using DEM-CFD. *Advanced Powder Technology*, *35*(5), Article 104432. https://doi.org/10.1016/j.apt.2024.104432

Advanced Powder Technology 35 (2024) 104432

Contents lists available at ScienceDirect

Advanced Powder Technology

journal homepage: www.elsevier.com/locate/apt

Original Research Paper

Effects of particle size distribution and blast velocity on furnace raceway transport behaviors and dynamic characteristics using DEM-CFD

Meng Li [a], Chao Li [b], Guanyin Wu [b], Xizhong An [a,*], Hao Zhang [a], Haitao Fu [a], Xiaohong Yang [a], Qingchuan Zou [a], Yongli Wu [c], Kejun Dong [d]

[a] Key Laboratory for Ecological Metallurgy of Multimetallic Mineral of Ministry of Education, School of Metallurgy, Northeastern University, Shenyang 110819, PR China
[b] Bayuquan Iron and Steel Branch, Angang Steel Company Limited, Yingkou 115007, PR China
[c] Faculty of Civil Engineering & Geosciences, Delft University of Technology 2628 CN Delft, the Netherlands
[d] School of Engineering, Design and Built Environment, Western Sydney University, 2751 Penrith, NSW, Australia

ARTICLE INFO

Article history:
Received 5 March 2024
Received in revised form 28 March 2024
Accepted 5 April 2024

Keywords:
Raceway dynamics
Transport behavior
Blast furnace
Particle size distribution
DEM-CFD

ABSTRACT

An in-depth exploration of the reaction kinetics and thermo-chemical behaviors of the raceway can offer practical insights for optimizing the operations of blast furnace (BF), thus achieving a more effective iron and steel production process. In this study, the dynamic characteristics and the flow, heat and mass transfer behaviors in the BF raceway were simulated by Discrete Element Method-Computational Fluid Dynamics (DEM-CFD) method at a particulate scale. The effects of coke size distribution and blast velocity on coke combustion characteristics, thermochemical behavior (particle volume fraction, raceway size, carbon loss, and coke temperature) and microscopic properties (coordination number (CN), contact normal force, pore structure and stress) were systematically investigated. The results show that as the blast velocity decreases or the size ratio λ (the largest coke particle size divided by the smallest coke particle size) increases, the raceway size becomes smaller, resulting in a smaller area of high oxygen (O_2) concentration and low carbon monoxide (CO) concentration in the raceway, and higher CO concentration in the packed bed. For the thermal-chemical behaviors, a lower blast velocity or a higher λ value decreases the number of particles experiencing mass loss, as well as increases individual particle mass loss, the average coke temperature and its variance. For microscopic properties, the CN distribution becomes wider as λ increases. The contact normal force in the coke bed with $\lambda > 1$ is significantly higher than that of $\lambda = 1$. As λ increases or blast velocity decreases, the pore distribution curve shifts to the left and the average pore volume decreases. The stress acting on the particles in the raceway increases with the blast velocity or λ. These new understandings of the complex reactive flow behaviors in the raceway will shed light on energy utilization and process optimization.

1. Introduction

The blast furnace (BF) is a huge reactor that transforms iron ores into molten iron, which is a crucial equipment in the iron and steel industry. Due to the high temperature condition and the huge size of BF, its operation is very energy-intensive and can cause substantial greenhouse gas (GHG) emissions. Statistics indicate that BF accounts for more than 70 % energy consumption [1,2] and nearly 90 % CO_2 emissions [3] in iron and steel plants. Therefore, it is critical to optimize the operation of BF for achieving a more energy-efficient and low-carbon production process [4].

In the BF production, hot air is normally blown through the surrounding tuyeres, resulting in the formation of the raceway. Basically, the raceway has significant influences on the BF performance in various aspects, e.g., the gas composition, the stability of the furnace, the formation of the softening-melting zone, and the reaction of the dripping zone [5–7]. Hence, the effective understanding on raceway is crucial for optimizing the performance of BF.

In the past decades, many scientists and engineers have been devoted to improving the understanding of the raceway through both experimental and numerical studies. Because of the high temperature, huge size, as well as the complex multiphase flows and thermochemical reactions, experimental studies on BF can be both challenging and expensive, thus have only been investigated by a

* Corresponding author.
E-mail address: anxz@mail.neu.edu.cn (X. An).

https://doi.org/10.1016/j.apt.2024.104432

few researchers. At room temperature, Sastry et al. [8,9] conducted lateral blowing experiments by using quartz sand and polypropylene particles, and they found that the particle properties have significant effects on the formation and rupture of the raceway. Wright et al. [10] investigated the formation mechanism of the raceway by comparing the effects of two-dimensional (2D) and three-dimensional (3D) modelling, conventional and non-conventional operations, and particle shapes. Nagomi et al. [11] proposed a model of the raceway based on 3D Computed Tomography (CT), which described in detail the spatial structure of the raceway and particle velocities. In addition, several studies at high temperatures were also performed. For example, Matsui et al. [12] used microwave reflection to measure the formation of the raceway at a high coal injection rate. Zhou et al. [13,14] investigated the combustion behavior of the raceway using a flame detection approach based on digital imaging and image processing techniques. It is known that physical experiments can provide insights into the evolution of the BF raceway and obtain information (*e.g.*, temperature and pressure) about the furnace operation at the macroscopic scale. However, it is difficult to comprehensively and precisely characterize the detailed microscopic information of gases and individual particles, such as velocities, forces, and gas composition.

In comparison, numerical simulations can be effective for generating detailed information on the particle/gas flow dynamics, heat and mass transfer, and chemical reaction processes in the BF, thus offering fundamental understanding for aiding the optimization of BF. In previous studies, two types of numerical approaches are generally adopted to describe the particle–fluid flow dynamics and thermochemical behaviors in the raceway: Two-Fluid Model (TFM) and Discrete Element Method-Computational Fluid Dynamics (DEM-CFD) model [15,16]. The TFM approach treats both the fluid phase and the particle phase as continuous media interpenetrating each other and solves the conservative equations of mass, momentum, and energy at computational cells with the incorporation of the kinetic theory of granular flow, which can simulate the large-scale particle–fluid systems at a relatively low computational cost [17]. Using TFM, many researchers investigated the effects of operation parameters on the raceway size and gas/solid motion [18,19] and the pulverized coal injection [20–27]. However, as a continuum and macroscopic approach, TFM cannot precisely provide the microscopic information at the particle scale, such as particle trajectories, particle residence time, and particle–particle/particle–fluid interactions that can be related to the strong collisions between particles in the raceway and the quasi-static flow of particles in the deadman region [28,29]. To solve these problems, researchers adopted the DEM-CFD model to study the behavior of the raceway in recent years. As shown in Table 1, the current researches based on the CFD-DEM method to investigate the behavior of blast furnace raceway can be divided into three levels [30–46]. Level 1: simulation of gas–solid flow under normal temperature and pressure; level 2: gas–solid two-phase flow simulation considering flow and heat transfer; level 3: gas–solid two-phase flow simulation that completely considers the flow, heat, mass transfer and chemical reaction phenomena. From level 1 to level 3, the model is updated iteratively and becomes more and more complex, which makes the CFD-DEM simulation of the BF raceway closer to the actual process. However, it is worth noting that the particles in the simulations considering flow heat and mass transfer were mainly assumed to be mono-sized, which is different from the multi-sized raw materials used in the actual BF. In addition, the effects of blast parameters and particle properties on the thermochemical behaviors of the raceway and the corresponding micromechanisms are still not fully understood.

In this study, the multiphase reacting flow, including heat and mass transfer, in the BF raceway were simulated by DEM-CFD method, which considers the reactions of coke combustion and carbon solution loss from the particle scale. First, the numerical model and simulation conditions were validated by comparing the simulation results and literature data. Then, the effects of blast velocity and particle size distribution on coke combustion characteristics (including gas species distributions and reaction kinetic rate) in the raceway were investigated. In addition, the thermochemical behaviors (particle volume fraction, raceway size, carbon loss, and coke temperature) in the raceway were systematically analyzed and their correlations with different process parameters were quantified. Finally, the mechanism of the coke combustion behavior was revealed by characterizing the microscopic properties such as coordination number, contact normal force, pores, and stresses. The obtained results are expected to provide insightful guidance for practical BF operation.

2. Numerical method and simulation conditions

2.1. Governing equations

In the utilized CFD-DEM model, the continuum fluid is described by the local averaged Navier-Stokes equations, and the motion of each particle is tracked by DEM. In DEM, the normal force is based on the classical Hertz's theory [47] and the tangential force is based on the Mindlin and Deresiewicz simplifications [48] with the Hertz-Mindlin no-slip model [49]. For gas-particle interaction, the drag force model proposed by Gidaspow [17] is used based on Wen and Yu [50] and Ergun [51]. All the governing equations and formulas describing the particle and fluid motion are summarized in Table 2. Four heat transfer models are considered in this study, namely particle–particle conduction, particle–fluid convection, particle-ambient radiation, and chemical reaction heat, details of the governing equations are listed in Table 3. In addition, the kinetic/diffusion-limited model, proposed by Field [60] and Baum and Street [61], is used to describe the reaction rate, in which the models of kinetic or diffusion rates are given in Table 4. The full nomenclature is given in Table A1 of Appendix A.

2.2. Simulation conditions and model validation

The raceway is the direct power source for the BF, which undergoes complex physical changes and chemical reactions. Generally, to reduce the computational cost, a slot model with gas blasted from the lateral side is used to simulate the raceway, which has been validated in many studies in terms of capturing and detecting motion characteristics [6]. As shown in Table 5, two reactions, including coke combustion ($C + O_2 \rightarrow CO_2$) and coke solution loss ($C + CO_2 \rightarrow 2CO$), are considered in the raceway. The relevant kinetic parameters required in the simulations are also included. And it should be noted that this study is based on all coke operation and does not consider coal combustion. Fig. 1 presents the computational geometry and meshes as well as the morphology of the coke bed, where the length, height, and thickness of the domain are 200 mm, 600 mm, and 18 mm, respectively. The tuyere with 6×10 mm^2 is located at a height of 65 mm from the bottom of the domain on the left wall of the bed.

For the solid phase, all the particles are spheres following Gaussian distributions as shown in Fig. 2. The particle size ranges from $\mu - 2\sigma$ to $\mu + 2\sigma$, where μ and σ are average particle size and the standard deviation of coke particles, respectively. In this study, the average particle size μ is 5 mm, and to facilitate the analysis, the size ratio λ, defined as the diameter ratio of the largest to the

Table 1
Summary of DEM-CFD simulations on the BF raceway.

Year	Authors	Objectives	Main achievements
2000	Xu et al. [30]	Simulations of gas–solid flow	Found that differences in lateral gas velocities lead to two manifestations of raceway and fluidization in the beds
2003	Feng et al. [31]		Investigated the gas/solid flow patterns and kinetic mechanisms of raceway formation
2006	Nouchi et al. [32]		Simulated solid flow and stress distributions in BF and analyzed the effects of hearth depth and burden load on coke free space
2010	Adema et al. [33]		Developed a model to describe the solid burden flow and the formation, shape, structure and permeability of cohesive zone
2022	Kamble et al. [34]		Analyzed the effects of gas velocity, particle material/size, the flux and size of coal on the raceway shape and size
2022	Nijssen et al. [35]		Studied the effects of burden weight, bi-disperse packing, blocked tuyeres on liquid/solid flow in the hearth using a full-3D model
2019	Wei et al. [36]	Coupled simulations of flow and heat transfer	Compared the heat transfer characteristics and microstructure of raceway for particles of prolate/oblate ellipsoids and spheres and found raceway size of prolate ellipsoidal particles is the smallest
2020	Wei et al. [37]		Studied the effects of gas velocity and particle shape on the raceway evolution, microstructure, temperature and bed porosity
2020	Wei et al. [38]		Investigated the influence of tetrahedron-like and octahedron-like particles on the microstructure and heat transfer of BF
2022	Wei et al. [39]		Explored the changing laws of BF raceway morphology and pressure drop with cylindrical particles
2020	Hou et al. [40]	Simulations of integrated flow, heat and mass transfer	Developed a model to predict the flow pattern, temperature distribution and iron ore reduction characteristics in BF
2020	Cui et al. [41]		Simulated the effects of gas velocity, particle size, bed height, and discharge rate on the flow and thermochemical behaviors of raceway
2021	Wang et al. [42]		Proposed a model to characterize the raceway dynamics and coke combustion and quantified the effect of operating parameters
2022	E et al. [43]		Explored the effects of blast parameters on raceway evolution and formation, microscale properties and coke combustion
2023	E et al. [44]		Studied the dynamics, microstructure and thermochemical behaviors in raceways of BF with hydrogen injection operations
2023	Aminnia et al. [45]		Developed a 3D model that incorporates gas–solid reacting flow to examine the coke combustion and heat distribution in raceway
2023	Xu et al. [46]		Simulated three adjacent raceways inside an industrial-scale BF

Table 2
Governing equations and formulas describing the particle and fluid motion.

Governing equations of fluid motion [52]	$\frac{\partial}{\partial t}\left(\varepsilon\rho_g\right)+\nabla\left(\varepsilon\rho_g\boldsymbol{u}_g\right)=S_{mf}$	(1)	Continuity equation
	$\frac{\partial}{\partial t}\left(\varepsilon\rho_g\boldsymbol{u}_g\right)+\nabla\left(\varepsilon\rho_g\boldsymbol{u}_g\boldsymbol{u}_g\right)=-\nabla p+\nabla\left(\varepsilon\bar{\bar{\tau}}\right)-S_p+\varepsilon\rho_g\boldsymbol{g}$	(2)	Momentum conservation equation
	$\tau=(\mu+\mu_t)\left[\nabla\boldsymbol{u}_g+\nabla\boldsymbol{u}_g^T-\frac{2}{3}\nabla\boldsymbol{u}_g I\right]$	(3)	Viscous stress tensor
	$S_p=\frac{\sum_{i=1}^{np}\left(F_{d,i}+F_{LS,i}+F_{LM,i}\right)}{\Delta V}$	(4)	Momentum sink
Fluid-particle interaction force [17]	$\boldsymbol{F}_{d,i}=\frac{\beta}{\rho_g}\left(\boldsymbol{u}_g-\boldsymbol{v}_{pi}\right)$	(5)	Drag force on an individual particle
	$\beta=\begin{cases}\frac{\mu(1-\varepsilon)}{\varepsilon d_p^2}\left[150(1-\varepsilon)+1.75Re_p\right], \varepsilon\le 0.8\\ \frac{3}{4}C_D\frac{\mu(1-\varepsilon)}{d_p^2}\varepsilon^{-2.7}Re_p, \varepsilon>0.8\end{cases}$	(6)	Gas–solid interphase drag coefficient
	$C_D=\begin{cases}\frac{24}{Re_p}\left(1+0.15Re_p^{0.687}\right), Re_p\le 1000\\ 0.43, Re_p>1000\end{cases}$	(7)	Drag coefficient for a single sphere
	$Re_p=\frac{\varepsilon\rho_g\left\|\boldsymbol{u}_g-\boldsymbol{v}_{pi}\right\|d_p}{\mu}$	(8)	Reynolds number calculation formula
Governing equations of particle motion	$m_i\frac{d\boldsymbol{v}_{pi}}{dt}=\boldsymbol{F}_{d,i}+\boldsymbol{F}_{LS,i}+\boldsymbol{F}_{LM,i}+\sum_{j=1}^{k}\boldsymbol{F}_{C,ij}+m_i\boldsymbol{g}$	(9)	Newton's second law of translational motion
	$I_i\frac{d\boldsymbol{w}_{pi}}{dt}=\sum_{j=1}^{k}\left(\boldsymbol{T}_{ij}^t+\boldsymbol{T}_{ij}^n\right)$	(10)	Newton's second law of angular motion
	$m_ic_i\frac{dT_i}{dt}=\sum_j\left(q_{i,j}+q_{i,conv}+q_{i,reac}+q_{i,rad}\right)$	(11)	Energy conservation equation
	$\boldsymbol{F}_{C,ij}=\boldsymbol{F}_{c,ij}^n+\boldsymbol{F}_{c,ij}^t+\boldsymbol{F}_{d,ij}^n+\boldsymbol{F}_{d,ij}^t$	(12)	Contact force
	$\boldsymbol{F}_{LS,i}=1.615\left(\boldsymbol{u}_g-\boldsymbol{v}_{pi}\right)\left(\rho_g\mu_g\right)0.5d_p^2C_{LS}\sqrt{\left\|\frac{\partial\boldsymbol{u}_g}{\partial n}\right\|}\mathrm{sgn}\left(\frac{\partial\boldsymbol{u}_g}{\partial n}\right)$	(13)	Saffman lift force [53]
	$\boldsymbol{F}_{LM,i}=\frac{1}{8}\rho g\left\|\boldsymbol{v}_r\right\|2\pi d_p^2C_{LM}\frac{\boldsymbol{w}_r\boldsymbol{v}_r}{\left\|\boldsymbol{w}_r\right\|\left\|\boldsymbol{v}_r\right\|}$	(14)	Magnus lift force [54]

smallest coke particles, with the range of 1.0–––4.0 is selected to replace the standard deviation σ. It should be noted that coke beds with λ = 1 are made up of mono-sized particles. The height of the coke bed with λ = 1 is 300 mm, and the weight of the coke bed for the other λ is the same as that for λ = 1 to avoid its influence on the simulation results. Periodic boundary condition is applied in the thickness direction to eliminate wall effects. Poisson's ratio, friction coefficients and restitution coefficient of coke particles are referred to the work of E et al. [43], and the detailed physical and numerical parameters used in the simulations are listed in Table 6. To ensure the reliability of the simulation results, the DEM time step is set to 30 % of the Rayleigh time step which is given by [64,65]:

$$T_R=\pi R\left(\frac{\rho}{G}\right)^{1/2}(0.1631\upsilon+0.8766)^{-1} \tag{25}$$

Table 3
Governing equations of four heat transfer models.

Particle-particle conduction [55]	$q_{i,j} = h_{i,j}(T_i - T_j)$	(15)
	$h_{i,j} = 2k_i\left[\frac{3F_i^n r^*}{4E^*}\right]^{1/3}$	(16)
Particle-fluid convection [37,56,57]	$q_{i,conv} = h_{i,conv} \cdot A_i \cdot (T_g - T_i)$	(17)
	$h_{i,conv} = 6(1-\varepsilon)k_i Nu/d_i^2$	(18)
	$Nu = \begin{cases} 2 + 0.6\varepsilon^{3.5}\mathrm{Re}_p^{1/2}\mathrm{Pr}^{1/3} & (\mathrm{Re}_p \le 200) \\ 2 + 0.5\varepsilon^{3.5}\mathrm{Re}_p^{1/2}\mathrm{Pr}^{1/3} + 0.02\varepsilon^{3.5}\mathrm{Re}_p^{0.8}\mathrm{Pr}^{1/3} & (200 < \mathrm{Re}_p < 1500) \\ 2 + 0.000045\varepsilon^{3.5}\mathrm{Re}_p^{1.8} & (\mathrm{Re}_p \ge 1500) \end{cases}$	(19)
Particle-ambient radiation [58,59]	$q_{i,rad} = \sigma\varepsilon_e A_i\left(T_{local,i}^4 - T_i^4\right)$	(20)
Chemical reaction heat [60]	$q_{i,reac} = -\Delta H_{reac}$	(21)

Table 4
Governing equations of the reaction model.

Kinetic/Diffusion-limited model [61,62]	$D_0 = C_1\frac{[(T_i+T_\infty)/2]^{0.75}}{d_i}$	(22)	Diffusion rate
	$R = C_2 e^{-(E/R_1 T)}$	(23)	Kinetic rate
	$\frac{dm_i}{dt} = -A_i p_{ox}\frac{D_0 R}{D_0 + R}$	(24)	Reaction rate

Table 5
The chemical reactions and related kinetic parameters used in the simulations [63].

Reactions	Equations	Pre-exponential factor, s^{-1}	Activation Energy, kJ/mol
Reaction 1	$C + O_2 \rightarrow CO_2$	1225	$9.977*10^7$
Reaction 2	$C + CO_2 \rightarrow 2CO$	7351	$1.380*10^8$

where R is the particle radius; ρ is the particle density; G is the shear modulus and υ is the Poisson's ratio. So the DEM time steps in the granular systems with different size distributions are 4.02×10^{-5} s, 3.28×10^{-5} s, 2.70×10^{-5} s, 2.05×10^{-5} s, and 1.58×10^{-5} s, respectively. As for the CFD time step, the previous study proved that the CFD time step should be 1–100 times the DEM time step in the CFD-DEM coupling [66]. Therefore, the CFD time step of 10^{-3} s was adopted in this work. The Courant number in the raceway is 12.9–13.8 by referring to the formula of the Courant number [67]. It should be noted that the implicit method to calculate the volume fraction in the Eulerian model, so the values of the Courant number are more generous compared to the explicit method. In addition, to analyze the sensitivity of Young's modulus, Fig. 3(a) shows the effect of Young's modulus on the spatial distribution of particle diameter and temperature in the raceway when u_g = 132 m/s and λ = 1. It is found that the raceway size becomes smaller with the increase of Young's modulus, and when the Young's modulus exceeds 10^7 Pa, the raceway size and particle diameter/temperature do not change significantly. Therefore, the value of Young's modulus is chosen as 10^7 Pa in this work. For the gas phase, hot air is introduced from the tuyere with a fixed velocity, pressure outlet boundary condition is employed on the upper surface of the domain, and the no-slip condition is applied at the wall. The fluid flow is determined by the standard k-ε turbulent model. The domain is divided into uniform grid cells, and the mesh independence in the simulation is verified by varying the number of meshes, as shown in Fig. 3(b), where three grid domains were tested, containing 2070, 3600 and 5550 CFD cells, respectively. The difference between the molar fraction distributions obtained with different grid cells is not significant. Thus, the computational domain containing 3600 CFD cells is chosen in this work. The effectiveness of DEM-CFD model is verified by comparing gas compositions along the central axis of the tuyere with those obtained in others' physical experiments [68] and numerical simulations [43], as shown in Fig. 3(c). Clearly, satisfactory agreement can be observed, implying the effectiveness and accuracy of our numerical model.

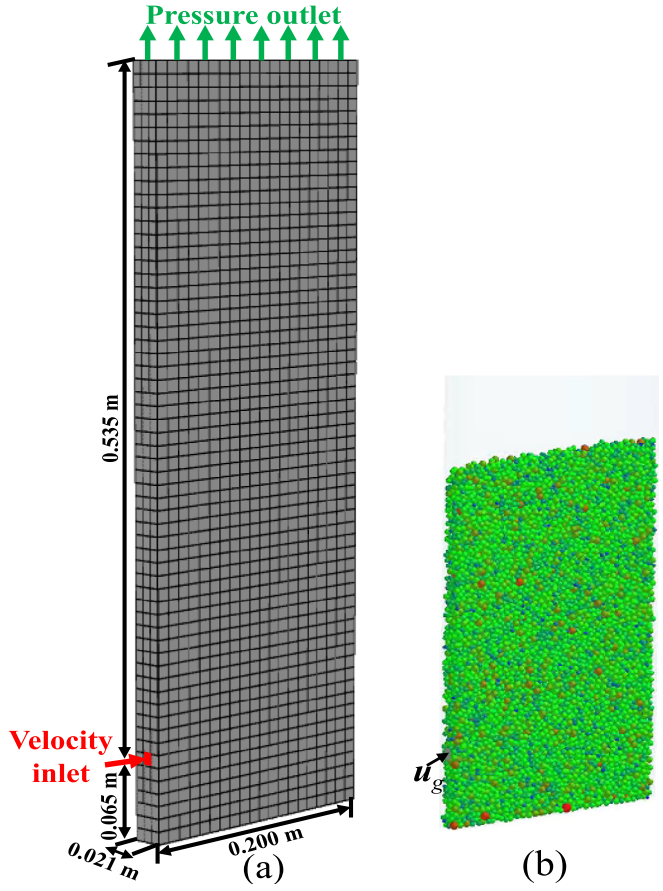

Fig. 1. (a) Schematic diagram of computational geometry and meshes; (b) initial packing of the coke bed.

3. Results and discussion

3.1. Coke combustion characteristics

The combustion and reaction processes occurring within the raceway affect the distribution of the gas components. Fig. 4 depicts the distribution of the molar fractions of each gas component (including O_2, CO) in the raceway under different blast velocities and λ. It should be emphasized that the analysis in this study is mainly based on the area around the tuyere due to the fact that the reactions of carbon combustion and the carbon-solution loss

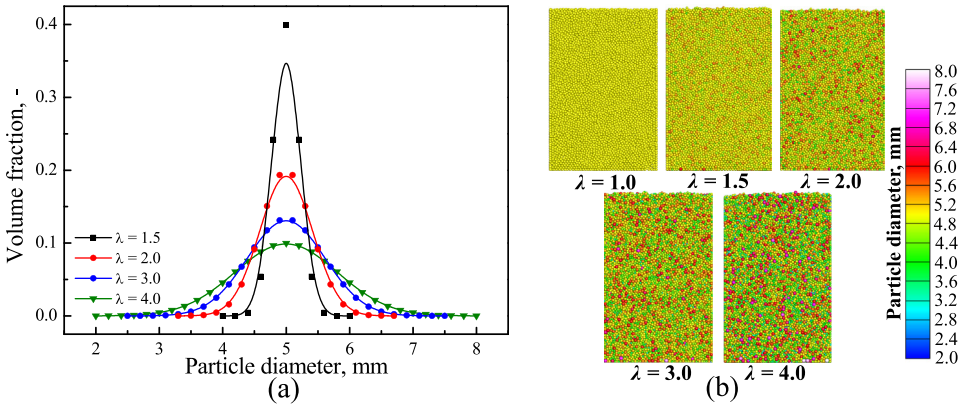

Fig. 2. (a) Particle size distributions used in the simulations, where the mean size μ = 5 mm and the λ varies from 1.0 to 4.0; (b) morphologies of the formed coke beds with different λ.

Table 6
Particle and fluid parameters used in the simulations [43].

Parameters	Values	Parameters	Values
Diameter of coke particle, d_p	2–8 mm	Blast velocity, u_g	129–138 m/s
Density of coke particles, ρ_p	1020 kg/m^3	Blast temperature, T_g	1273 K
Number of coke particles, N	9056–10789	Oxygen concentration, –	0.21
Initial temperature of coke particle, $T_{initial}$	800 K	Gas density, ρ_g	1.2 kg/m^3
Thermal conductivity of coke particles, k_{coke}	1.7 W/m·K	Gas dynamic viscosity, μ_g	1.8e-5 kg/m·s
Specific heat capacity of coke particles, c_{coke}	850 J/kg·K	Gas thermal conductivity, k_g	0.0262 W/m·K
Restitution coefficient, e	0.8	Gas specific heat capacity, c_g	1006 J/kg·K
Particle-particle/wall sliding friction coefficient, μ_s	0.4	Emissivity, ε_e	0.8
Particle-particle/wall sliding friction coefficient, μ_r	0.05	Fluid time step, $\triangle t_f$	0.001 s
Young's modulus of coke particle, E	10^7 kg/m·s^2	Solid time step, $\triangle t_s$	1.58×10^{-5} s-4.02×10^{-5} s
Poisson ratio of coke particle, υ	0.3		

hardly occur in the upper region of the coke bed. When high-temperature O_2 is injected into the raceway from the tuyere, the coke particles around the tuyere experience intense combustion due to the high oxygen concentration, which results in the release of a large amount of heat and CO_2 around the raceway. Subsequently, CO_2 is converted to CO by the carbon-solution loss reaction with the coke. As the reaction continues, the produced CO fills the entire coke bed, causing its concentration in the coke bed to far exceed the raceway. In addition, the regions of high O_2 concentration and low CO concentration close to the tuyere decrease in sizes with the decrease of blast velocity and the increase of λ by comparing the molar fraction distributions of O_2 and CO for different λ or blast velocities.

Considering and controlling the gas molar fraction distribution along the tuyere are essential for designing and optimizing the combustion system. Fig. 5 illustrates the molar fraction distribution of gas species (O_2, CO) along the central axis of the tuyere for different blast velocities and λ. As λ increases or blast velocity decreases, the size of the raceway decreases, and the faster the variation rate of O_2/CO molar fractions along the tuyere. This is mainly due to the lower bed porosity formed at the wider size distribution or the smaller blast velocity, and thus the hot air is not easy to diffuse in the bed. Such change can also be revealed from the subsequent characterization of the pore sizes of the bed. In addition, a larger λ leads to a higher molar fraction of CO in the coke bed due to more carbon loss of coke in this case, resulting in a larger amount of CO due to more coke gasification. This can also be confirmed by the subsequent analysis of the mass loss in the coke bed.

Understanding and controlling the interaction between the distributions of gas components and the kinetic rates of the reactions in BF is important to optimize the reaction process and enhance production efficiency. The kinetic rate distributions for Reaction 1 and Reaction 2 under different blast velocities and λ are shown in Fig. 6. It can be seen that the kinetic rates of the reactions are concentrated in the annular region around the cavity of the raceway. The kinetic rate reaches the maximum at the position along the central axis of the tuyere due to the strong interaction of mass, momentum, and energy between gas and solid phases. In addition, the raceway size increases due to the increase of the blast velocity and the decrease of λ, thus the annular region where the reactions occur gradually expands. Fig. 7 shows the distribution of kinetic rates along the central axis of tuyere for Reaction 1 and Reaction 2 at different blast velocities and λ. The distribution curve shifts to the right with increasing blast velocity and decreasing λ. However, it should be noted that the peaks of kinetic rates along the central axis of the tuyere do not show an obvious pattern, which is mainly because the reaction kinetic rates are related to particle sizes. The particles are always in the annular flow in the raceway, resulting in different spatial distributions of coke particles with different sizes at different moments.

3.2. Thermo-chemical behavior

The particle volume fraction of the coke bed is of great importance to the smelting and operational stability of the BF. The heat transfer and combustion performance of the BF can be improved by appropriately controlling the volume fraction of the coke bed. The raceway size directly affects the burden flow and the reaction process in the BF. Fig. 8(a) depicts the spatial distribution of particle volume fraction in the coke bed at different blast velocities and λ. The region of the coke bed where the particle volume fraction is lower than 0.3 is recognized as the raceway [44]. The center section along the direction of thickness was used to estimate the raceway size in this study. From the figures it can be seen that the raceway size becomes larger with the increase of the blast velocity and the decrease of λ, and the effect of coke size distribution on the raceway size is not obvious when λ exceeds 3.

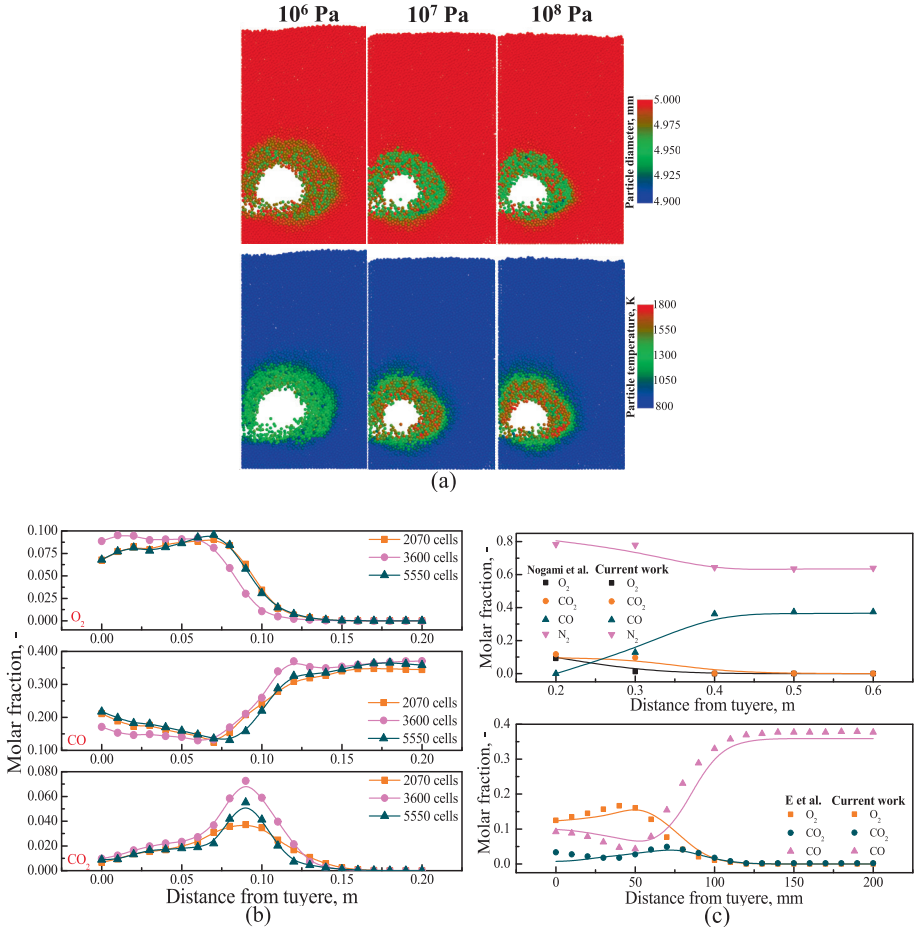

Fig. 3. (a) Effect of Young's modulus on the spatial distribution of particle diameter and temperature in the raceway when u_g = 132 m/s and λ = 1; (b) gas species distributions along the tuyere axis with different mesh divisions; (c) comparison of gas compositions along the central axis of the tuyere in the current work with the results of Nogami et al. [68] and E et al. [43].

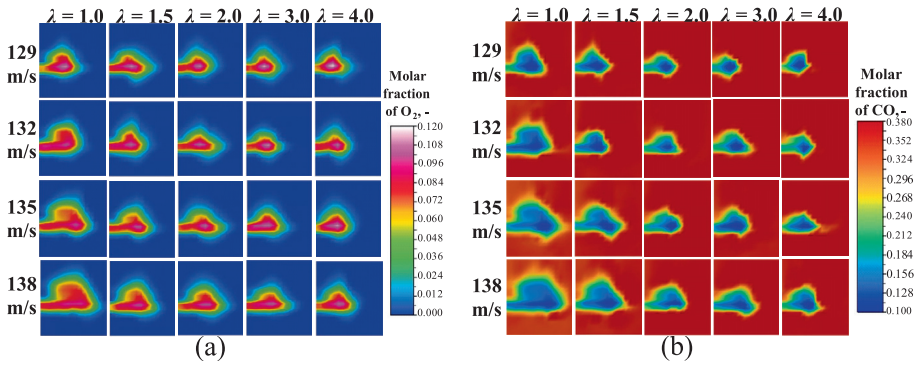

Fig. 4. Spatial distributions of the gas species of O_2 (a) and CO (b) under different blast velocities and λ.

To clearly characterize the interphase interaction between gas and solid in the BF, the spatial distribution of particle mass loss in coke bed under various blast velocities and λ are investigated in Fig. 9. The results show that the number of particles undergoing mass loss in the coke bed increases with the increase of blast velocity or the decrease of λ, but the mass loss of individual particles decreases. The mass loss probability distributions and total mass loss in the coke bed under different conditions are shown in Fig. 10(a) and (b). The disturbance of gas within the raceway is intensified with the increase in the blast velocity, which leads to a violent movement of coke particles and hence more coke particles being involved in the raceway. The width of the mass loss probability distribution hardly varies with the blast velocity, but its peak value increases with the blast velocity, which leads to an increase in the total mass loss of the coke bed. When λ increases, the average pore size of the coke bed decreases, limiting the gas flow through the coke bed and enhancing the species transport of individual coke particles. As a result, the mass loss probability

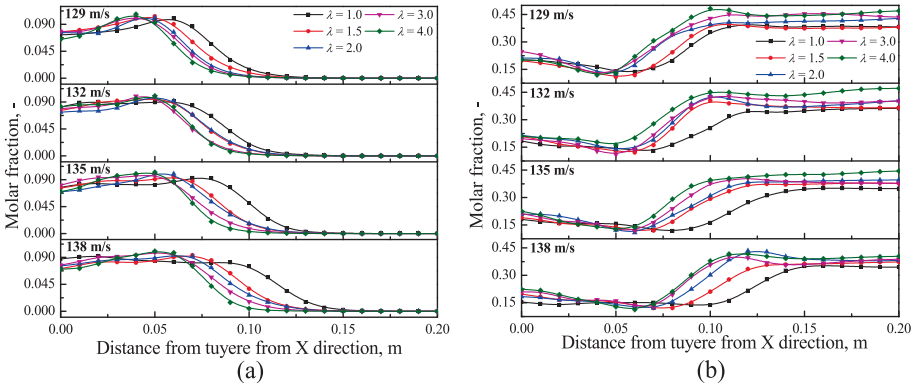

Fig. 5. Molar fraction distributions of O_2 (a) and CO (b) along the central axis of the tuyere under various blast velocities and λ.

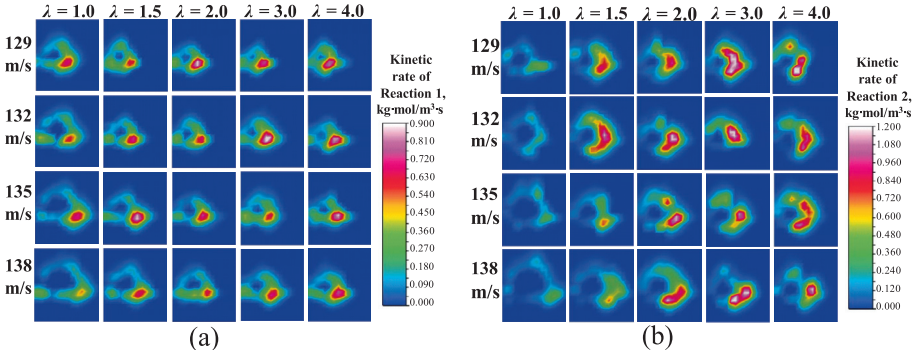

Fig. 6. Spatial distributions of the kinetic rates of Reaction 1 (a) and Reaction 2 (b) under different blast velocities and λ.

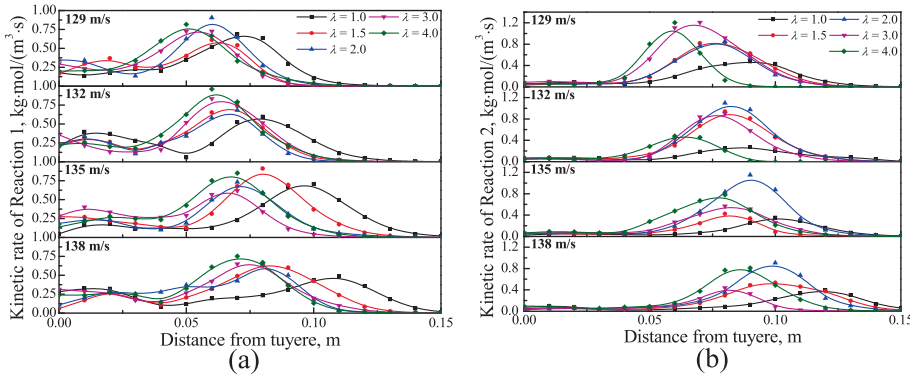

Fig. 7. Kinetic rates distributions of the gas species for Reaction 1 (a) and Reaction 2 (b) along the central axis of the tuyere under different blast velocities and λ.

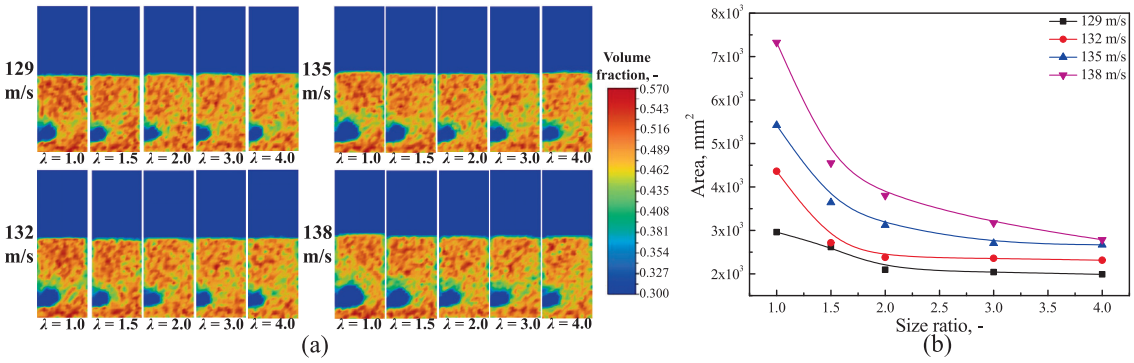

Fig. 8. (a) Spatial distributions of particle volume fraction of coke beds under different blast velocities and λ; (b) variations of the raceway area with λ for different blast velocities in the center section of the coke bed.

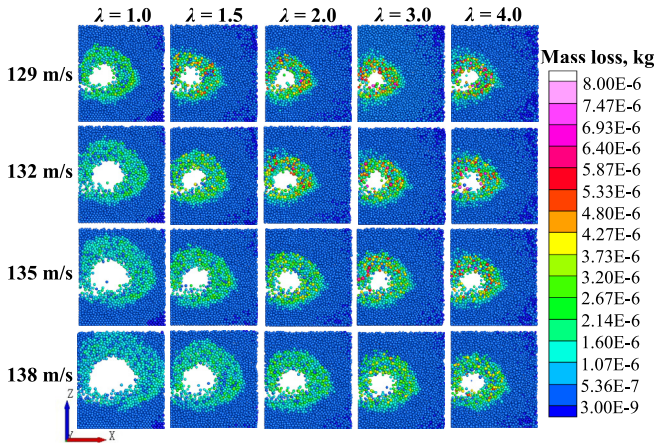

Fig. 9. Spatial distributions of particle mass loss in the coke bed under different blast velocities and λ.

distribution curve widens and its peak value decreases. In addition, the wider the coke size distribution, the more total mass loss of the coke bed.

The temperature of coke particles in the raceway has a significant influence on the reaction rate and homogeneity of smelting in the BF. In this study, the temperature distributions of coke particles in the raceway are analyzed under different blast velocities and coke size distributions, as shown in Fig. 11(a). It can be seen that the smaller the blast velocity or the larger λ, the higher the temperature of coke particles, which is consistent with the distribution of the mass loss. This is mainly due to more intense gasification reaction occurring to the particles, and hence more reaction heat is generated. In addition, Fig. 11(b) analyzes the average temperature and the variance of coke particles in the raceway. It can be seen that the average temperature of the coke particles and its variance increase with the decrease of the blast velocity or the increase of λ. Besides, the increase rate of the average temperature and its variance both decrease with the increase of λ.

Fig. 12(a) further presents the probability distributions of particle temperature under different blast velocities and λ. It can be seen that the width of the probability distribution of particle temperature does not change significantly with the blast velocity, while its peak increases with the increase of the blast velocity. In addition, the wider coke size distribution leads to more inhomogeneous combustion and heat transfer of coke particles, which in turn induces wider width and lower peak of the probability distribution of particle temperature in the raceway. The relationship between the carbon loss and temperature of coke particles in the BF indeed exists, which is affected by a variety of factors such as temperature, size distribution of coke particles, and so on. Fig. 12 (b) explores the relationship between the coke temperature and the mass loss for different particle size distributions and blast velocities. It can be observed that the particle temperature increases slowly as further carbon is lost from the coke, which is mainly due to the fact that the organic matter inside the coke is gradually consumed to form charcoal ash covering the surface of the coke particles with the combustion and gasification of coke, thus reducing the rate of combustion and gasification, and therefore resulting in the limitation of heat transfer [69]. In addition, the wider the particle size distribution, the faster the particle temperature rises with carbon loss of coke, owing to the greater number of smaller-sized particles in the wider particle size distribution. Smaller particles have a larger area to react with gases due to their larger specific surface area, and the chemical reaction rate is faster, resulting in a faster increase in temperature.

3.3. Microstructure analysis

The design and optimization of microstructures are of great significance to the operation and smelting efficiency of the BF. By rationally designing the microstructure, the gas and hot air can be fully mixed within the raceway to improve combustion efficiency. The coordination number (CN) is closely related to the connectivity and heat transfer of granular matter, which is a basic and important parameter to describe the packing structure. Fig. 13(a) and (b) depict the spatial and probability distributions of CN in the coke bed under different blast velocities and λ, respectively. It can be seen that the large raceway leads to the presence of more freely moving particles, resulting in a higher proportion of particles with CN = 0 at the larger blast velocity. The overall CN distribution curve does not change significantly with the blast velocity. In addition, the CN distribution becomes wider as λ increases.

The force between particles is an important parameter to characterize the internal structure of the BF. By monitoring and analyzing the variation of contact normal forces, the particle collision, fragmentation and erosion processes under different process conditions can be studied and understood. The spatial distributions of contact normal force in the coke granular system under different λ and blast velocities are given in Fig. 14(a), where the color and thickness of the "bars" represent the magnitude of the contact nor-

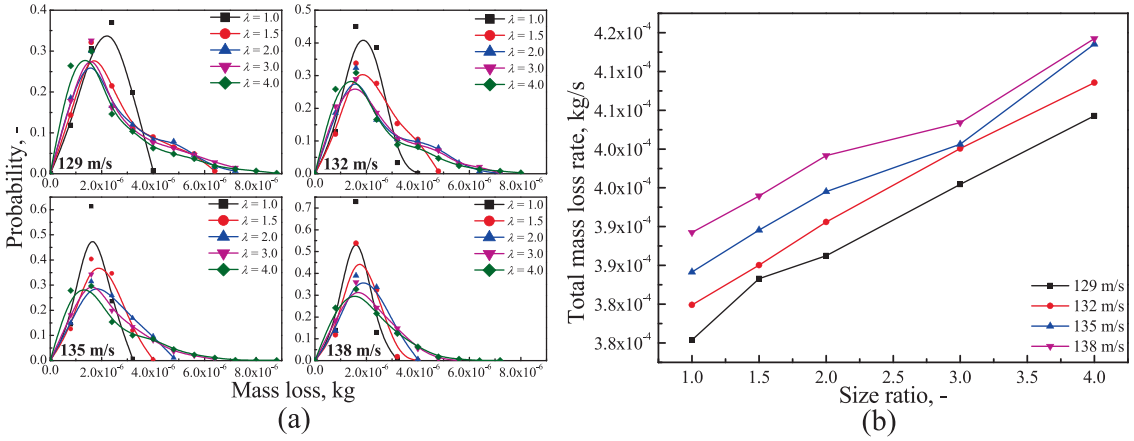

Fig. 10. (a) Probability distributions of mass loss under various blast velocities and λ; (b) variations of total mass loss in the coke bed with the size ratio λ under different blast velocities.

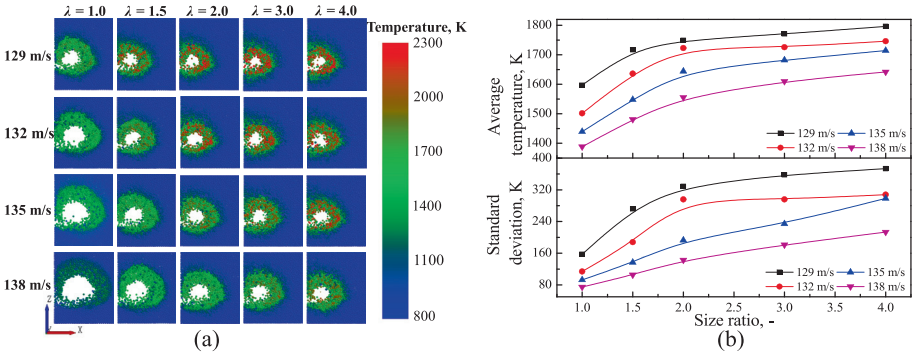

Fig. 11. (a) Distributions of particle temperature and particle volume fraction of coke bed under different blast velocities and λ; (b) variation of the mean and standard deviation of particle temperature with λ under different blast velocities.

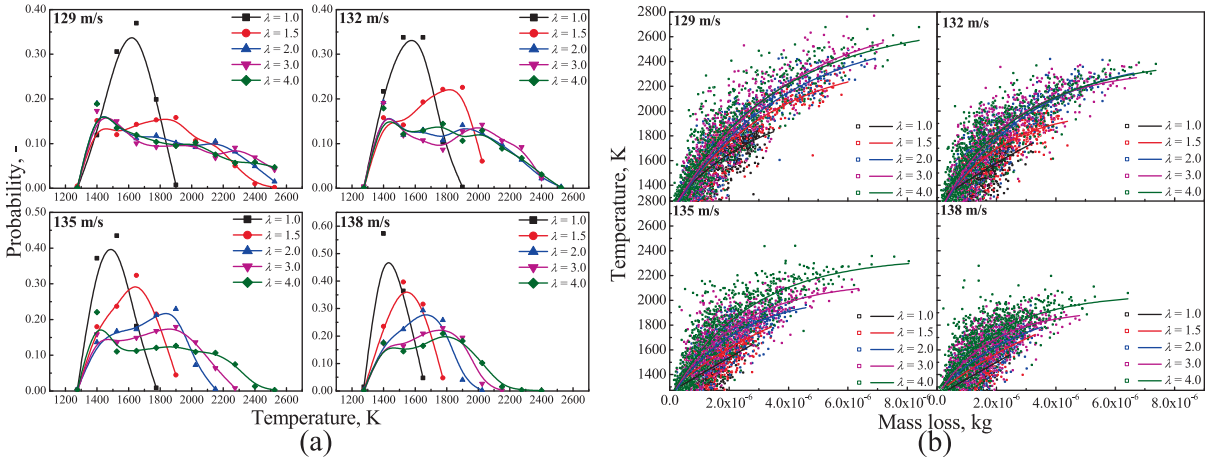

Fig. 12. (a) Probability distributions of particle temperature under different blast velocities and λ; (b) relationships between particle temperature and its mass loss under different blast velocities and λ.

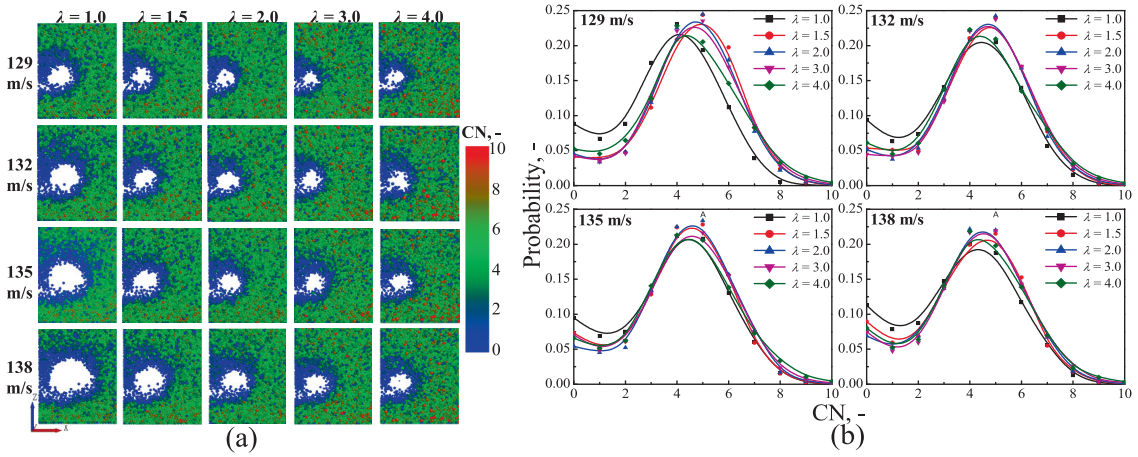

Fig. 13. Spatial profiles (a) and probability distributions (b) of CN under different blast velocities and λ.

mal force between particles. Those large contact normal forces are mainly concentrated around the raceway due to the intense collision between the circulating and stagnant particles at the boundary of the raceway, which is transmitted to the surrounding particles in a net-like pattern. The weaker contact normal forces are mainly distributed in the loose packing region above the raceway. Fig. 14(b) shows the probability distribution of contact normal force in the coke particle system under different λ and blast velocities. The probability distributions of contact normal forces for other λ are significantly larger compared to that for $\lambda = 1$, which is also verified in the results of Huang et al. [70]. In addition, when $\lambda > 1$, the probability distributions do not show the obvious difference, owing to two reasons: the increase of λ leads to the smaller raceway, which weakens the gas–solid interaction and makes the contact normal force decrease, and the collisions between larger and smaller particles result in the larger normal contact forces.

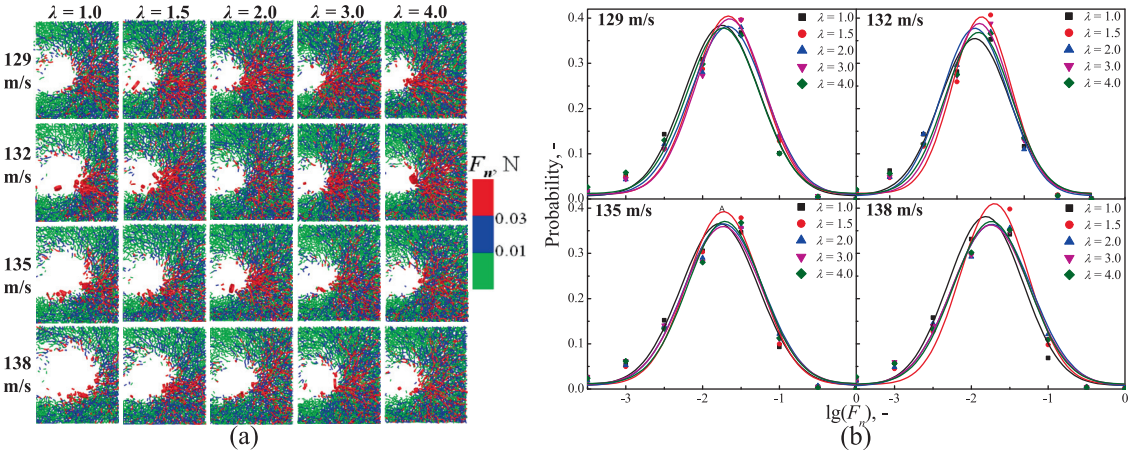

Fig. 14. Spatial (a) and probability (b) distributions of contact normal forces under different blast velocities and λ.

Understanding the information of pore structure, distribution and channel connectivity in the raceway is essential for optimizing the tuyere design and improving the distribution and permeability of the gas. In this section, the pore structure of the coke bed is analyzed by using the Radical Tessellation (RT), which is suitable for the quantitative characterization of pores formed by particles with different sizes [71–73]. This method divides the entire packing bed into a group of non-overlapping convex Polyhedra (RPs), where each RP contains one particle. Thus, the pore size V_c around each particle in a RP can be calculated by:

$$V_c = V_{rp} - V_p \tag{25}$$

where V_c is the volume of the pore in each RP; V_{rp} is the volume of the RP; and V_p is the volume of the particle in the RP. A larger V_c represents a larger volume of pore around a particle.

Fig. 15(a) shows the visualization of the RT network of the coke bed obtained under various blast velocities and λ. Fig. 15(b) and (c) depict the effects of blast velocity and λ on the pore volume distribution. As illustrated in the figures the peak of each curve is mainly distributed in the range of 40–50 mm^3. For a given blast velocity, as λ increases, the pore volume distribution shifts to the left, implying small porosity in the bed, which is mainly because small particles can fill the pores formed by large particles as a general phenomenon in the packing of multi-sized particles [74]. On the other

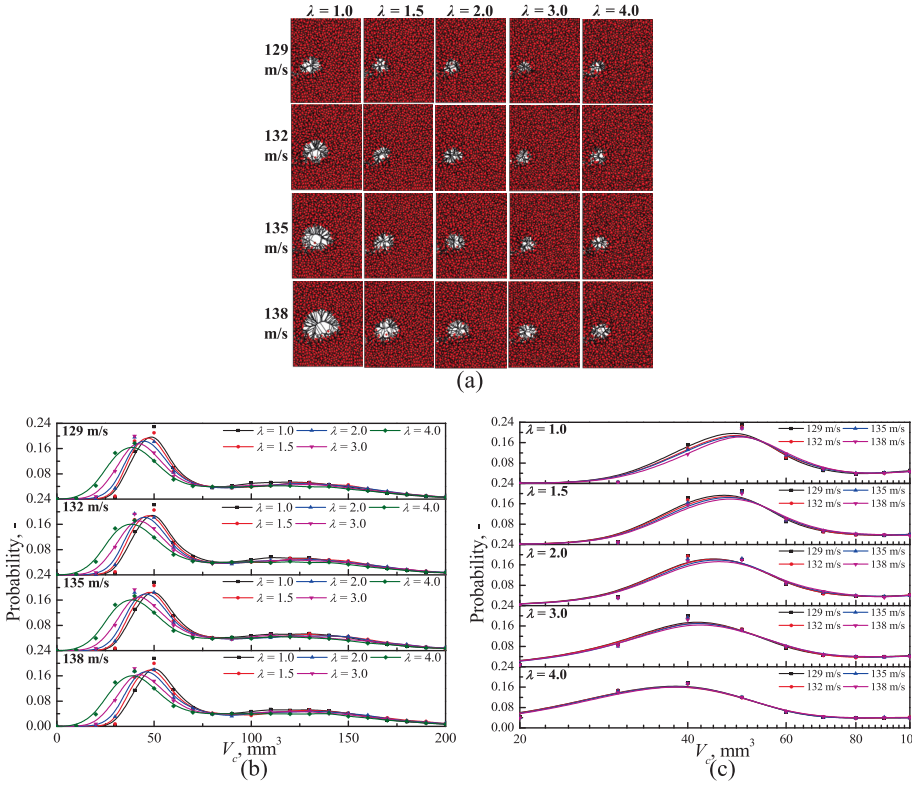

Fig. 15. (a) The visualization of RT networks of coke beds formed under different conditions; pore size distributions in the coke beds under different λ (b) and blast velocities (c).

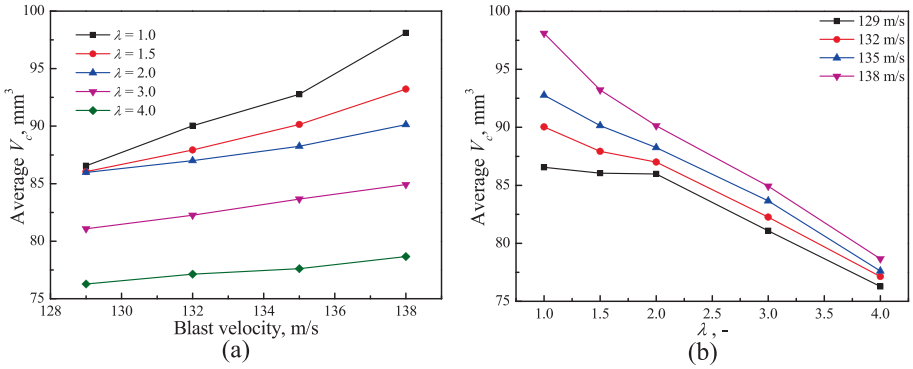

Fig. 16. Influences of the blast velocity (a) and λ (b) on the average pore size.

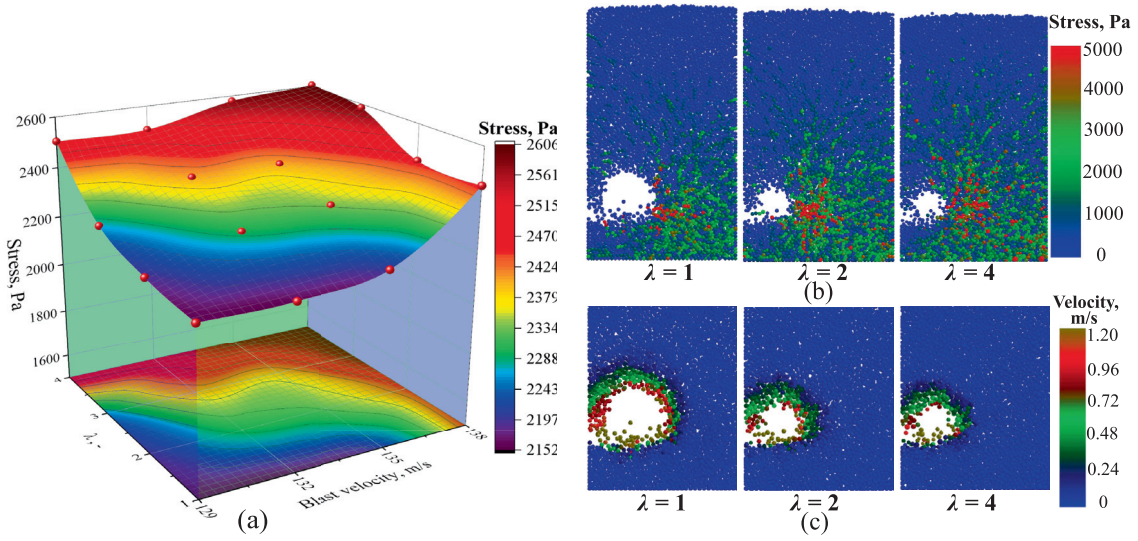

Fig. 17. (a) Effect of blast velocity and λ on the mean stress; spatial distributions of stress (b) and velocity (c) in the coke bed with different λ.

hand, for a fixed particle size distribution, increasing blast velocity causes the pore volume distribution shifting to the right and the porosity in the bed increasing. When λ is larger than 2, the pore volume distribution curve does not change significantly with blast velocity, which is because the particles with a wider size distribution are easier to be rearranged to fill the voids in the bed when perturbed by the hot air. Fig. 16 illustrates the effects of blast velocity and λ on the average pore volume. It can be seen that the average pore volume increases with blast velocity and the growth rate of the pore volume is slower as λ increases. The average pore volume decreases with the increase of λ, and the growth rate of the pore volume is not obviously changed with the blast velocity.

The mechanical stresses on the particle surfaces in the raceway are derived from the impact force of gas flow, and particle collision force. Fig. 17(a)-(b) analyzes the spatial distribution of stresses at different λ, as well as the effects of blast velocity and λ on the average stress. It can be seen that a higher λ or blast velocity corresponds to a higher stress in the raceway. This is mainly because the main source of stress comes from the impact force of the airflow. Thus, the stress in the coke bed increases with the blast velocity. At the same blast velocity, the smaller the average pore volume of the packing structure with wider coke size distribution restricts the gas flow and increases the interaction between the particles, which leads to an increase in the stress acting on the particles and a decrease in the particle velocity. This is also illustrated in the analysis of the particle velocities in the raceway in Fig. 17(c).

4. Conclusions

The kinetic characteristics and flow, heat and mass transfer behaviors in the raceway of BF were simulated by DEM-CFD method, in which the chemical reactions including coke combustion and carbon solution loss were considered. The effects of coke size distribution and blast velocity on coke combustion characteristics, thermochemical behavior and microstructure were systematically investigated, and the corresponding mechanism was analyzed. The main conclusions are as follows:

1. For combustion characteristics, the variation rate of O_2/CO along the axis of tuyere becomes faster with the increase of λ or the decrease of blast velocity. Besides, the reaction kinetic rate is mainly concentrated in the annular region around the raceway cavity, and this region expands with increasing blast velocity and decreasing size ratio λ.

2. With the increase of blast velocity and the decrease of λ, the raceway size becomes larger. In addition, when the λ exceeds 3, the effect of coke size distribution on the raceway size is not obvious.
3. For the thermal-chemical behaviors, as the blast velocity decreases or λ increases, the number of particles in the coke bed undergoing mass loss decreases, but the mass loss of individual particles becomes larger, the temperature of coke particles rises more obviously, and the average coke temperature and its variance increase. However, the total mass loss increases with the blast velocity or λ. In addition, the probability distribution of temperature does not vary significantly with the blast velocity, but its peak value increases with the blast velocity. At a larger λ, the temperature probability distribution is wider and the peak is lower. And the increase rate of coke temperature with carbon loss is faster.
4. For microstructure, the overall CN distribution does not change significantly when blast velocity increases, except for the higher proportion of particles with CN = 0. The CN distribution becomes wider as λ increases. The large contact normal forces are mainly concentrated around the raceway, and the weaker contact normal forces are mainly distributed in the loose packing region above the raceway. The contact normal forces in the coke bed with $\lambda > 1$ are significantly higher than those of $\lambda = 1$. As λ increases or blast velocity decreases, the pore distribution curve shifts to the left and the average pore volume decreases. When the λ is larger than 2, increasing the blast velocity has little effect on the pore distribution of the bed. The stress acting on the particles in the raceway increases with the blast velocity or λ.

CRediT authorship contribution statement

Meng Li: Conceptualization, Data curation, Formal analysis, Investigation, Methodology, Validation, Writing – original draft. **Chao Li:** Conceptualization, Data curation, Resources, Validation, Writing – review & editing. **Guanyin Wu:** Formal analysis, Methodology, Resources, Visualization, Writing – review & editing. **Xizhong An:** Conceptualization, Formal analysis, Funding acquisition, Methodology, Project administration, Resources, Supervision, Writing – review & editing. **Hao Zhang:** Formal analysis, Investigation, Software, Visualization, Writing – review & editing. **Haitao Fu:** Conceptualization, Formal analysis, Methodology, Validation, Writing – review & editing. **Xiaohong Yang:** Conceptualization, Investigation, Resources, Writing – review & editing. **Qingchuan Zou:** Conceptualization, Formal analysis, Methodology, Resources, Writing – review & editing. **Yongli Wu:** Data curation, Methodology, Software, Visualization, Writing – review & editing. **Kejun Dong:** Formal analysis, Methodology, Resources, Software, Writing – review & editing.

Declaration of competing interest

The authors declare that they have no known competing financial interests or personal relationships that could have appeared to influence the work reported in this paper.

Acknowledgements

The authors acknowledge the National Natural Science Foundation (51374070) and Liaoning Revitalization Talents Program (XLYC1805007) of China for the financial support.

Appendix A

Table A1
Nomenclature

Symbols	Descriptions	Symbols	Descriptions
ε	Fluid volume fraction, –	m_i	Particle mass, kg
ρ_g	Gas density, kg/m^3	$\boldsymbol{\omega}_{pi}$	Particle angular velocity, rad/s
$\boldsymbol{u}_g$	Gas velocity, m/s	$\boldsymbol{T}_{ij}^t$	Tangential torque, kg/m^2
p	Static pressure, Pa	$\boldsymbol{T}_{ij}^n$	Normal torque, kg/m^2
$\boldsymbol{g}$	Gravity acceleration, m/s^2	C_{LS}	Saffman lift coefficient, –
μ	Gas dynamic viscosity, N·s/m^2	C_{LM}	Magnus lift coefficient, –
μ_t	Turbulent viscosity, N·s/m^2	$\boldsymbol{v}_r$	Relative velocity, m/s
ΔV	Volume of computational cell, m^3	$\boldsymbol{w}_r$	Relative angular velocity, rad/s
$\boldsymbol{v}_{pi}$	Particle translational velocity, m/s	$\boldsymbol{H}$	Displacement vector, m
d_p	Particle diameter, m	t	Time, s
I_i	Inertial moment, kg/m^2	T_i	Particle temperature, K
k_i	Thermal conductivity, W/(m·K)	A_i	Particle surface area, m^2
F_i^n	Particle normal force, N	T_g	Fluid temperature, K
E^*	Effective particle radius, m	Nu	Nusslet number, –
σ	Stefan-Boltzmann constant, –	ε_e	Particle emissivity, –
C_1	The diffusion rate constant, –	C_2	Pre-exponential factor, s^{-1}
E	Activation energy, J/mol	R_1	Gas constant, 8.314 J/(mol·K)
$T_{local,i}$	Average particle–fluid temperature, K	p_{ox}	The partial pressure of the oxidant, Pa

References

[1] Y. Omori, Blast Furnace Phenomena and Modeling, Elsevier Applied Science, London, 1987.
[2] J.A. de Castro, C. Takano, J. Yagi, A theoretical study using the multiphase numerical simulation technique for effective use of H2 as blast furnaces fuel, J. Mater. Res. Technol. 6 (2017) 258–270.
[3] C.B. Xu, D.C. Cang, A brief overview of low CO_2 emission technologies for iron and steel making, J. Iron Steel Res. Int. 17 (2010) 1–7.
[4] W.Q. Sun, Q. Wang, Y. Zhao, J.Z. Wu, Material and energy flows of the iron and steel industry: status quo, challenges and perspectives, Appl. Energy 268 (2020) 114946.

[5] Y.S. Shen, B.Y. Guo, S. Chew, P. Austin, A.B. Yu, Three-dimensional modeling of flow and thermochemical behavior in a blast furnace, Metall. Mater. Trans. B 46 (2015) 432–448.
[6] J. Hilton, P. Cleary, Raceway formation in laterally gas-driven particle beds, Chem. Eng. Sci. 80 (2012) 306–316.
[7] Q.F. Hou, D.Y. E, S.B. Kuang, Z.Y. Li, A.B. Yu, DEM-based virtual experimental blast furnace: a quasi-steady state model, Powder Technol. 314 (2017) 557–566.
[8] G.S.S.R.K. Sastry, G.S. Gupta, A.K. Lahiri, Void formation and breaking in a packed bed, ISIJ Int. 43 (2003) 153–160.
[9] G.S.S.R.K. Sastry, G.S. Gupta, A.K. Lahiri, Cold model study of raceway under mixed particle conditions, Ironmaking Steelmaking 30 (2003) 61–65.
[10] B. Wright, P. Zulli, Z.Y. Zhou, A.B. Yu, Gas-solid flow in an ironmaking blast furnace-I: physical modelling, Powder Technol. 208 (2011) 86–97.
[11] H. Nogami, H. Kawai, J. Yagi, Measurement of three-dimensional raceway structure in small scale cold model by X-ray computed tomography, Tetsu to Hagane 100 (2014) (2014) 256–261.
[12] Y. Matsui, Y. Yamaguchi, M. Sawayama, S. Kitano, N. Nagai, T. Imai, Analyses on blast furnace raceway formation by microwave reflection gunned through tuyere, ISIJ Int. 45 (2005) 1432–1438.
[13] D.D. Zhou, S.S. Cheng, R.X. Zhang, Y. Li, T. Chen, Uniformity and activity of blast furnace hearth by monitoring flame temperature of raceway zone, ISIJ Int. 57 (2017) 1509–1516.
[14] D.D. Zhou, S.S. Cheng, Measurement study of the PCI process on the temperature distribution in raceway zone of blast furnace by using digital imaging techniques, Energy 174 (2019) 814–822.
[15] X.F. Dong, A.B. Yu, J.I. Yagi, P. Zulli, Modelling of multiphase flow in a blast furnace: recent developments and future work, ISIJ Int. 47 (2007) 1553–1570.
[16] S.B. Kuang, Z.Y. Li, A.B. Yu, Review on modeling and simulation of blast furnace, Steel Res. Int. 89 (2018), 1700071.
[17] M. Banaei, J. Jegers, M.V. Annaland, J.A.M. Kuipers, N.G. Deen, Tracking of particles using TFM in gas-solid fluidized beds, Adv. Powder Technol. 29 (2018) 2538–2547.
[18] S.S. Mondal, S.K. Som, S.K. Dash, Numerical predictions on the influences of the air blast velocity, initial bed porosity and bed height on the shape and size of raceway zone in a blast furnace, J. Phys. d: Appl. Phys. 38 (2005) 1301–1307.
[19] D. Rangarajan, T. Shiozawa, Y.S. Shen, J.S. Curtis, A.B. Yu, Influence of operating parameters on raceway properties in a model blast furnace using a two-fluid model, Ind. Eng. Chem. Res. 53 (2014) 4983–4990.
[20] Y.S. Shen, B.Y. Guo, A.B. Yu, P. Zulli, A three-dimensional numerical study of the combustion of coal blends in blast furnace, Fuel 88 (2009) 255–263.
[21] A. Hideyuki, N. Hiroshi, T. Hideo, M. Takatoshi, F. Takeshi, Simulation of transport the blast furnace with phenomena and without around the raceway zone in pulverized coal injection, ISIJ Int. 33 (1983) 646–654.
[22] M.Y. Gu, M.C. Zhang, N.K.C. Selvarasu, Y.F. Zhao, C.Q. Zhou, Numerical analysis of pulverized coal combustion inside tuyere and raceway, Steel Res. Int. 79 (2008) 17–24.
[23] M.Y. Gu, G.A. Chen, M.C. Zhang, D. Huang, P. Chaubal, C.Q. Zhou, Three-dimensional simulation of the pulverized coal combustion inside blast furnace tuyere, Appl. Math. Model. 34 (2010) 3536–3546.
[24] Y.S. Shen, B.Y. Guo, A.B. Yu, D. Maldonado, P. Austin, P. Zulli, Three-dimensional modelling of coal combustion in blast furnace, ISIJ Int. 48 (2008) 777–786.
[25] Y.S. Shen, A.B. Yu, Modelling of injecting a ternary coal blend into a model ironmaking blast furnace, Miner. Eng. 90 (2016) 89–95.
[26] D.L. Wu, P. Zhou, H.J. Yan, P.Y. Shi, C.Q. Zhou, Numerical investigation of the effects of size segregation on pulverized coal combustion in a blast furnace, Powder Technol. 342 (2019) 41–53.
[27] Y.T. Zhuo, Y.S. Shen, Three-dimensional transient modelling of coal and coke co-combustion in the dynamic raceway of ironmaking blast furnaces, Appl. Energy 261 (2020) 114456.
[28] X.P. Qiu, L.M. Wang, N. Yang, J.H. Li, A simplified two-fluid model coupled with EMMS drag for gas-solid flows, Powder Technol. 314 (2017) 299–314.
[29] W.J. Yang, Z.Y. Zhou, A.B. Yu, Discrete particle simulation of solid flow in a three-dimensional blast furnace sector model, Chem. Eng. J. 278 (2015) 339–352.
[30] B.H. Xu, A.B. Yu, S.J. Chew, P. Zulli, Numerical simulation of the gas-solid flow in a bed with lateral gas blasting, Powder Technol. 109 (2000) 13–26.
[31] Y.Q. Feng, D. Pinson, A.B. Yu, S.J. Chew, P. Zulli, Numerical study of gas-solid flow in the raceway of a blast furnace, Steel Res. Int. 74 (2003) 523–530.
[32] T. Nouchi, T. Sato, M. Sato, K. Takeda, Stress field and solid flow analysis of coke packed bed in blast furnace based on DEM, Tetsu to Hagane 92 (2006) 955–960.
[33] A.T. Adema, Y.X. Yang, R. Boom, Discrete element method-computational fluid dynamic simulation of the materials flow in an iron-making blast furnace, ISIJ Int. 50 (2010) 954–961.
[34] S. Kamble, F.S.D. Bosco, G.S. Gupta, Effect of raceway shape and size on gas and fines flow behavior in a packed bed, Metall. Mater. Trans. B 53 (2022) 2117–2131.
[35] T.M.J. Nijssen, J.A.M. Kuipers, J. van der Stel, A.T. Adema, K.A. Buist, Large-scale VOF/CFD-DEM simulation of blast furnace hearth dynamics, ISIJ Int. 62 (2022) 1146–1158.
[36] G.C. Wei, H. Zhang, X.Z. An, B. Xiong, S.Q. Jiang, CFD-DEM study on heat transfer characteristics and microstructure of the blast furnace raceway with ellipsoidal particles, Powder Technol. 346 (2019) 350–362.
[37] G.C. Wei, H. Zhang, X.Z. An, D.Y. E, Numerical investigation on the mutual interaction between heat transfer and non-spherical particle dynamics in the blast furnace raceway, Int. J. Heat Mass Transfer 153 (2020) 119577.
[38] G.C. Wei, H. Zhang, X.Z. An, S.Q. Jiang, Influence of particle shape on microstructure and heat transfer characteristics in blast furnace raceway with CFD-DEM approach, Powder Technol. 361 (2020) 283–296.
[39] G.C. Wei, H. Zhang, X.Z. An, Q.F. Hou, Effect of particle shape on raceway size and pressure drop in a blast furnace: Experimental, numerical and theoretical analyses, Adv. Powder Technol. 33 (2022) 103455.
[40] Q.F. Hou, D.Y. E, S.B. Kuang, A.B. Yu, A transient discrete element method-based virtual experimental blast furnace model, Steel Res. Int. 91 (2020) 2000071.
[41] J.X. Cui, Q.F. Hou, Y.S. Shen, CFD-DEM study of coke combustion in the raceway cavity of an ironmaking blast furnace, Powder Technol. 362 (2020) 539–549.
[42] S. Wang, Y.S. Shen, CFD-DEM modelling of raceway dynamics and coke combustion in an ironmaking blast furnace, Fuel 302 (2021) 121167.
[43] D.Y. E, P. Zhou, S.Y. Guo, J. Zeng, Q. Xu, L.J. Guo, Q.F. Hou, A.B. Yu, Particle-scale study of coke combustion in the raceway of an ironmaking blast furnace, Fuel 311 (2022) 122490.
[44] D.Y. E, P. Zhou, L.Y. Ji, J.X. Cui, Q. Xu, L.J. Guo, A.B. Yu, Particle-scale modelling of injected hydrogen and coke co-combustion in the raceway of an ironmaking blast furnace, Fuel 336 (2023) 126778.
[45] N. Aminnia, P. Adhav, F. Darlik, M. Mashhood, S.H. Saraei, X. Besseron, B. Peters, Three-dimensional CFD-DEM simulation of raceway transport phenomena in a blast furnace, Fuel 334 (2023) 126574.
[46] D. Xu, S. Wang, Y.S. Shen, Numerical investigation of the reacting flows of three adjunct raceways in an industrial-scale blast furnace, Fuel 354 (2023) 129339.
[47] H. Hertz, Uber die beruhrung fester elastischer korper (on the contact of elastic solids), J. Reine Angew. Math. 92 (1882) 156–171.
[48] R.D. Mindlin, H. Deresiewicz, Elastic spheres in contact under varying oblique forces, J. Appl. Mech. 20 (1953) 327.
[49] B.K. Mishra, C. Thornton, An improved contact model for ball mill simulation by the discrete element method, Adv. Powder Technol. 13 (2002) 25–41.
[50] Y. Wen, Y.H. Yu, Mechanics of fluidization, Chem. Eng. Prog. Symp. Ser. 162 (1966) 100–111.
[51] S. Ergun, Fluid flow through packed columns, J. Mater. Sci. Chem. Eng. 48 (1952) 89–94.
[52] V. Agrawal, Y. Shinde, M.T. Shah, R.P. Utikar, V.K. Pareek, J.B. Joshi, Effect of drag models on CFD-DEM predictions of bubbling fluidized beds with Geldart D particles, Adv. Powder Technol. 29 (2018) 2658–2669.
[53] A. Zarghami, J.T. Padding, A. Drag, lift and torque acting on a two-dimensional non-spherical particle near a wall, Adv. Powder Technol. 29 (2018) 1507–1517.
[54] R.J. Liu, R. Xiao, M. Ye, Z.M. Liu, Analysis of particle rotation in fluidized bed by use of discrete particle model, Adv. Powder Technol. 29 (2018) 1655–1663.
[55] J.H. Fu, S. Chen, X.C. Zhou, Effect of heterogeneity on interphase heat transfer for gas-solid flow: a particle-resolved direct numerical simulation, Phys. Fluids 34 (2022) 123317.
[56] B. Chaudhuri, F.J. Muzzio, M.S. Tomassone, Modeling of heat transfer in granular flow in rotating vessels, Chem. Eng. Sci. 61 (2006) 6348–6360.
[57] J. Li, D.J. Mason, A computational investigation of transient heat transfer in pneumatic transport of granular particles, Powder Technol. 112 (2000) 273–282.
[58] Z.Y. Zhou, A.B. Yu, P. Zulli, Particle scale study of heat transfer in packed and bubbling fluidized beds, AIChE J. 55 (2009) 868–884.
[59] Q.F. Hou, Z.Y. Zhou, A.B. Yu, Computational study of heat transfer in a bubbling fluidized bed with a horizontal tube, AIChE J. 58 (2012) 1422–1434.
[60] K.I. Tanoue, T. Hinauchi, O.O. Thaung, T. Nishimura, M. Taniguchi, K.I. Sasauchi, Modeling of heterogeneous chemical reactions caused in pyrolysis of biomass particles, Adv. Powder Technol. 18 (2007) 825–840.
[61] M.A. Field, Rate of combustion of size-graded fractions of char from a low rank coal between 1200 K-2000 K, Combust. Flame 13 (1969) 237–252.
[62] M.M. Baum, P.J. Street, Predicting the combustion behavior of coal particles, Combust. Sci. Technol. 3 (1971) 231–243.
[63] T. Okosun, S. Street, J. Zhao, B. Wu, C. Zhou, Influence of conveyance methods for pulverised coal injection in a blast furnace, Ironmaking Steelmaking 44 (2017) 513–525.
[64] L.T. Zhu, Y.N. Luo, D.T. Pan, Z.H. Luo, Capability assessment of coarse-grid simulation of gas-particle riser flow using sub-grid drag closures, Chem. Eng. Sci. 213 (2020) 115410.
[65] H. Lei, L.T. Zhu, Z.H. Luo, CFD-DEM study of reactive gas-solid flows with cohesive particles in a high temperature polymerization fluidized bed, Chem. Eng. Sci. 268 (2023) 118437.
[66] D.Y. Liu, C.S. Bu, X.P. Chen, Development and test of CFD-DEM model for complex geometry: a coupling algorithm for fluent and DEM, Comput. Chem. Eng. 58 (2013) 260–268.
[67] L.T. Zhu, M. Ye, Z.H. Luo, Application of filtered model for reacting gas−solid flows and optimization in a large-scale methanol-to-olefin fluidized-bed reactor, Ind. Eng. Chem. Res. 55 (2016) 11887–11899.

[68] H. Nogami, H. Yamaoka, K. Takatani, Raceway design for the innovative blast furnace, ISIJ Int. 46 (2015) 1104–1111.
[69] K.J. Li, J.L. Zhang, Z.J. Liu, M. Barati, J.B. Zhang, M.F. Wei, G.W. Wang, K.X. Jiao, T. J. Yang, Interfaces between coke, slag, and metal in the tuyere level of a blast furnace, Metall. Mater. Trans. B 53 (2022) 2117–2131.
[70] H. Zhang, Y.Q. Huang, X.Z. An, A.B. Yu, J. Xie, Numerical prediction on the minimum fluidization velocity of a supercritical water fluidized bed reactor: effect of particle size distributions, Powder Technol. 389 (2021) 119–130.
[71] P. Richard, L. Oger, J.P. Troadec, A model of binary assemblies of spheres, Eur. Phys. J. E 6 (2001) 295–303.
[72] L. Wang, X.Z. An, D.F. Wang, Q. Qian, Topological and metrical property characterization of radical subunits for ternary hard sphere crystals, AIP Adv. 6 (2016) 015115.
[73] D.F. Wang, X.Z. An, D.Z. Gou, H.Y. Zhao, L. Wang, F. Huang, DEM construction of binary hard sphere crystals and radical tessellation, AIP Adv. 8 (2018) 105203.
[74] L.Y. Yi, K.J. Dong, R.P. Zou, A.B. Yu, Radical tessellation of the packing of spheres with a log-normal size distribution, Phys. Rev. E 92 (2015) 032201.